Proceedings of the ASME 2020 15th International Manufacturing Science and Engineering Conference
MSEC2020
June 22-26, 2019, Cincinnati, OH, USA

MSEC2020-8433

THERMAL MODELING IN METAL ADDITIVE MANUFACTURING USING GRAPH THEORY: EXPERIMENTAL VALIDATION WITH IN-SITU INFRARED THERMOGRAPHY DATA FROM LASER POWDER BED FUSION

Reza Yavari[1] , Richard Williams[2], Kevin Cole[1*], Paul Hooper[2] and Prahalada Rao[1]

[1]Mechanical and Materials Engineering, University of Nebraska-Lincoln,
Lincoln, NE 68588-0526, United States
[2]Department of Mechanical Engineering, Imperial College London, UK

ABSTRACT

The objective of this work is to provide experimental validation of the graph theory approach for predicting the thermal history in additively manufactured parts that was recently published in the ASME transactions. In the present paper the graph theory approach is validated with in-situ infrared thermography data in the context of the laser powder bed fusion (LPBF) additive manufacturing process. We realize this objective through the following three tasks. First, two types of test parts (stainless steel) are made in two corresponding build cycles on a Renishaw AM250 LPBF machine. The intent of both builds is to influence the thermal history of the part by changing the cooling time between melting of successive layers, called interlayer cooling time. Second, layer-wise thermal images of the top surface of the part are acquired using an in-situ *a priori* calibrated infrared camera. Third, the thermal imaging data obtained during the two builds were used to validate the graph theory-predicted surface temperature trends. Furthermore, the surface temperature trends predicted using graph theory are compared with results from finite element analysis. As an example, for one the builds, the graph theory approach accurately predicted the surface temperature trends to within 6% mean absolute percentage error, and approximately 14 Kelvin root mean squared error of the experimental data. Moreover, using the graph theory approach the temperature trends were predicted in less than 26 minutes which is well within the actual build time of 171 minutes.

Keywords: Additive Manufacturing, Thermal Modeling, Graph Theory, Validation, Laser Powder Bed Fusion, Infrared Thermal Measurements, Interlayer Cooling Time.

1 Introduction

The thermal history of an additively manufactured (AM) part as it is being built layer-upon-layer is a critical determinant of its functional integrity [1, 2]. Accurate and fast computational approaches to predict the thermal history in AM parts are valuable for: (i) reducing the experimental tests needed to optimize processing conditions; and (ii) augmenting in-process sensor data for closed-loop process control [3-8].

In a previous paper, we proposed a graph theory-based computational heat transfer approach for predicting the thermal history in AM parts in near real-time [9]. In that paper, the graph theory-predicted temperature trends were verified with: (a) exact analytical Green's function-based solutions, (b) finite element implementation of Goldak's double ellipsoid moving heat source model [10, 11], and (c) a commercial software for thermal simulation in AM (Autodesk Netfabb). Results from our prior work showed that the graph theory approach was about ten times faster than the benchmark Goldak's model implemented with the finite element method in Abaqus. The mean absolute percentage error of the graph theory-derived predictions relative to finite element analysis was less than 10%.

The objective of the present paper is to validate the graph theoretic approach using in-situ infrared thermal imaging data acquired in the specific context of the laser powder bed fusion (LPBF) AM process. In LPBF, metal powder is deposited on a bed (build plate) and selectively melted layer-upon-layer using a laser. The cyclical heating and cooling of the part during LPBF is one of the main causes for defects such as cracking and distortion in shape [2, 7].

[*] Corresponding author. Email: Tel.: +01-402-472-5857. *E-mail address:* kcole1@unl.edu

To realize the foregoing objective, we frame the following three tasks:

(1) Two distinctive test part geometries were made in two separate builds on a Renishaw AM250 LPBF system. The two test parts built were:
   (i) a cylinder of diameter 8 mm and height 60 mm deposited under a build plan that causes variation in the interlayer cooling time (ILCT), viz., the time between the end of melting a layer and the start of melting of the next layer for a specific location, and
   (ii) an inverted cone shape with bottom diameter of 2 mm, top diameter of 20 mm, and vertical build height of 11 mm, whose geometry leads to a gradual change in the ILCT.

(2) During the two aforementioned builds, temperature measurements of the top surface of the test parts were acquired using an in-situ longwave infrared camera (spectral range 7.5 μm to 13 μm). An offline calibration procedure was used to convert the relative temperature trends recorded by the infrared camera to absolute temperature scale.

(3) The temperature trends predicted using the graph theory-based approach was validated against the experimental measurements of the surface temperature of the part. The graph theory predictions were also compared with a finite element solution.

The rest of this paper is structured as follows. Section 2 describes the research methodology including the LPBF setup and experimental procedure to obtain surface temperature measurements with in-situ infrared thermal imaging for two builds. Section 2 also summarizes the approach used to calibrate and adapt the graph theory model for predicting the surface temperature trends. Validation of the graph theory-predicted surface temperature trends with experimental temperature observations and comparison with finite element analysis are reported in Section 3. Lastly, the conclusions and avenues for future work are summarized in Section 4.

2 Methods

2.1 Experimental Setup

The experimental setup and calibration process is detailed in a recent publication [12]; a brief summary is given here. As shown in Figure 1, a FLIR A35X longwave infrared (LWIR) camera with a spectral range of 7.5 μm to 13 μm is integrated within the build chamber of a Renishaw AM250 LPBF machine. The thermal camera is sealed inside a vacuum-tight box with a germanium window, and focused onto the build plate inclined at an angle of 66° from the horizontal. This configuration allows measurement of the surface temperature of the whole build area continuously throughout the process.

Thermal images are captured at a resolution of 320 × 256 pixels, providing a pixel resolution of approximately 1 mm^2, and recorded at a rate of 60 frames per second. To calibrate for absolute temperature, the data captured by the thermal camera was analyzed for a cylinder-shaped calibration artefact identical in geometry and material to one of the experimental test parts – Build 1 – described later in Sec. b. This calibration procedure, described in depth in Ref. [12], ensures that the surface characteristics, and hence emissivity of the calibration artifact are similar to the test parts used in this work. To summarize, the temperature of the calibration artefact is controlled using a cartridge heater embedded inside a built-in cavity. The surface temperature of the calibration artifact is recorded using thermocouples inside two slots on the top surface and mapped against readings of the LWIR thermal camera [12].

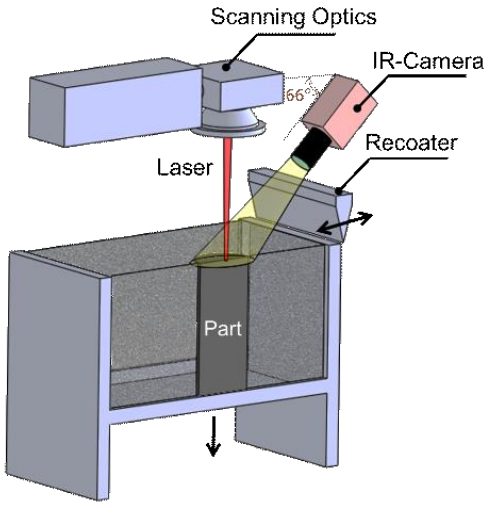

Figure 1: The schematic of the experimental setup used in this work; surface temperature data is acquired by a longwave infrared camera which is inclined at an angle of 66° to the horizontal plane.

2.2 Experimental Builds

a. Rationale

The three main factors that influence the temperature distribution in LPBF parts are [13]:

(1) The geometry of the part, including features such as steep overhangs, and the presence of anchoring supports [14-17]. The geometry of the part beneath the powder bed determines the rate at which the heat is conducted away from the build surface. Supports are an important aspect of the part geometry because they serve as conduits for heat to dissipate [7, 17].

(2) Type and characteristics of the feedstock material, and process parameters, such as the laser power, hatch spacing, layer thickness, laser scan velocity, and scanning strategy, which governs the average heat input for melting (global energy density).

(3) The time between the end of scanning of a layer and start of scanning of the next layer, called interlayer cooling time (ILCT), is a function of the build layout determined by the number, geometry, orientation, placement and scanning sequence of other parts on the build plate.

In this work, we conducted two builds that are designed to influence the surface temperature distribution in the test part through gradual variation in the ILCT. The scan pattern, process parameters and material properties for the two builds are reported in Table 1.

b. Build 1 – Inducing variation in the interlayer cooling time by altering the build plan.

The test part is cylinder of diameter 8 mm and height 60 mm in the center of the build plate. This cylindrical test part is built in three phases, as depicted in Figure 2. In Phase 1, the test part is built along with eight other identical cylinders arranged in a grid pattern. The ILCT in Phase 1 is roughly 10.5 seconds. After a build height of 20 mm (400 layers, each layer is 50 µm) is reached, the processing of the rest of the cylinders is stopped marking the end of Phase 1, and start of Phase 2. In Phase 2, only the test sample, i.e., the center cylinder is processed until a total build height of 40 mm (800 layers) is reached. Because only one cylinder is processed, the ILCT reduces to nearly 6.6 seconds from 10.5 seconds in Phase 1.

Lastly, in Phase 3, all nine cylinders are again processed for a total build height of 60 mm (1200 layers). Accordingly, in Phase 3, the ILCT again increases to approximately 10.5 seconds. The total build time is about 171 minutes. In Phase 3 because there is raw un-melted powder underneath the rest of the eight cylinders, the laser power for melting of these eight cylinders is set at a minimum of 5 W to avoid potential build failures given their unsupported geometry.

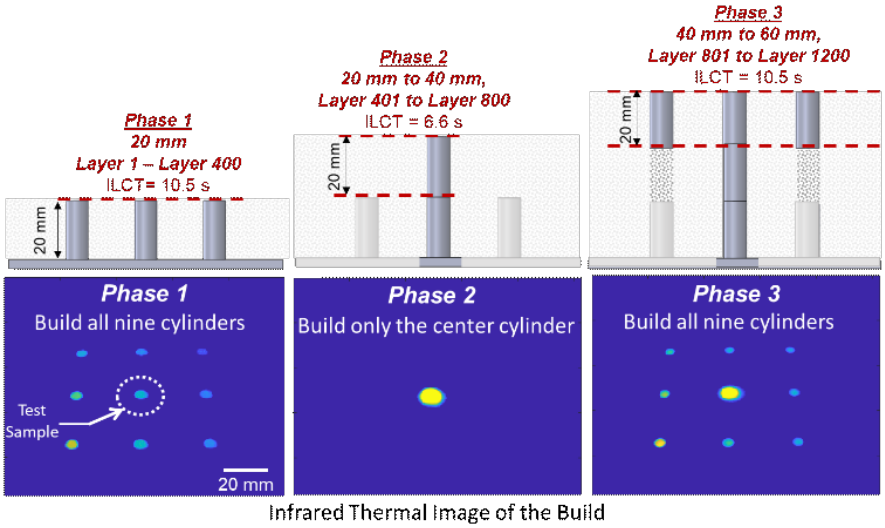

Figure 2. The three phases in building the cylinder part. Shown in the top is the front view, with the change in the interlayer cooling time (ILCT) depending on the number of parts being processed in a layer. Shown in the bottom is the corresponding infrared image of the part captured by the thermal camera.

Table 1. Summary of the material and processing parameters used in this work for Build 1 and 2.

Process Parameter	Values [units]
Laser type and wavelength.	200 W fibre laser wavelength 1070 nm
Laser power, point distance, exposure time	200 W, 60 um, 80 us
Inner border parameters - power, point distance, exposure time	200 W, 40 um, 90 us
Outer border parameters - power, point distance, exposure time	110 W, 20 um, 100 us
Hatch spacing	110 um
Layer thickness	50 um
Spot diameter of the laser	65 um
Scanning strategy for the bulk section of the part	Meander-type scanning strategy without rotation of scan path between layers.
Build atmosphere	Argon
Material Properties	Values [units]
Material type	316L stainless steel
Particle size	10-45 um

c. Build 2 – Inducing variation in the interlayer cooling time through the part geometry.

The test part devised for this build is shown in Figure 3; it is an inverted cone whose diameter gradually increases from 2 mm to 20 mm over a build height of 11 mm (50 µm layer thickness, 220 layers). The build time is about 51 minutes. In this test part, the ILCT increases almost linearly from 10 seconds to 16 seconds proportion to the build height, while the narrower cross-section of the part in the preceding layers impedes the diffusion of heat. Consequently, the temperature of the top surface increases progressively with the deposition of new layers.

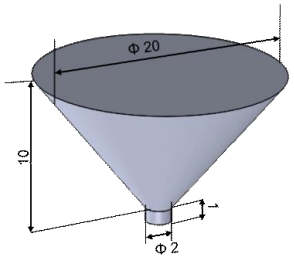

Figure 3. The schematic of the inverted cone geometry implemented in Build 2.

2.3 Pre-Processing the Temperature Measurements Acquired from the Thermal Camera

The surface temperature of a pixel located in the center of the thermal image of the test artifact is tracked throughout the process. This surface temperature signal reveals the presence of several sharp peaks. These peaks are artifacts that correspond to certain process events extraneous to the melting process. Referring to Figure 4(c) and (d), we extract the steady state surface temperature before melting of the new layer as the representative surface temperature. This aspect is common to both Build 1 and Build 2. We now describe the signal obtained.

Step 1: Large upward spike due to laser exposure.

In this stage of the process, the laser is active (ON), and is currently scanning the powder bed. The maximum temperature in the large upward peak results when the laser is exactly over that reference point on the powder bed that aligns with the IR camera pixel which is used to map the temperature trends. The temperature values in this step (large upward spikes) are not meaningful and accurate since the temperature values are beyond the calibrated temperature range of the IR camera. Moreover, the spatial and temporal resolution of the IR camera is not sufficient to resolve the temperature at the meltpool scale; the meltpool in LPBF is typically under 100 um, while the resolution of the IR camera used in this work is greater than 1 mm × 1 mm.

Step 2: First downward spike due to the recoater blocking the field-of-view of the IR camera when it returns to the powder reservoir.

After the end of sintering a layer, the recoater returns to fetch fresh powder. During Step 2, the bed is lowered so that the recoater can pass freely over the powder bed and avoid scraping the part. As the recoater returns to fetch fresh powder, it momentary blocks the IR camera field-of-view leading to a large downward spike in temperature lasting less than a 1/50th of a second.

Step 3: Second downward spike due to new powder being deposited on the powder bed when the recoater rakes a new layer of powder on the surface of build plate.

As the recoater makes another pass to deposit new powder, it momentarily blocks, again, the observation point from the field-of-view of the IR camera causing a large downward spike in the raw signal. Because, a fresh layer of powder material is deposited during this step, the recoater speed is considerably slower than in the previous Step 2, and hence the downward peak lasts for close to 1/5th of a second. Once the three large spikes have been removed the temperature trends are averaged over the ILCT.

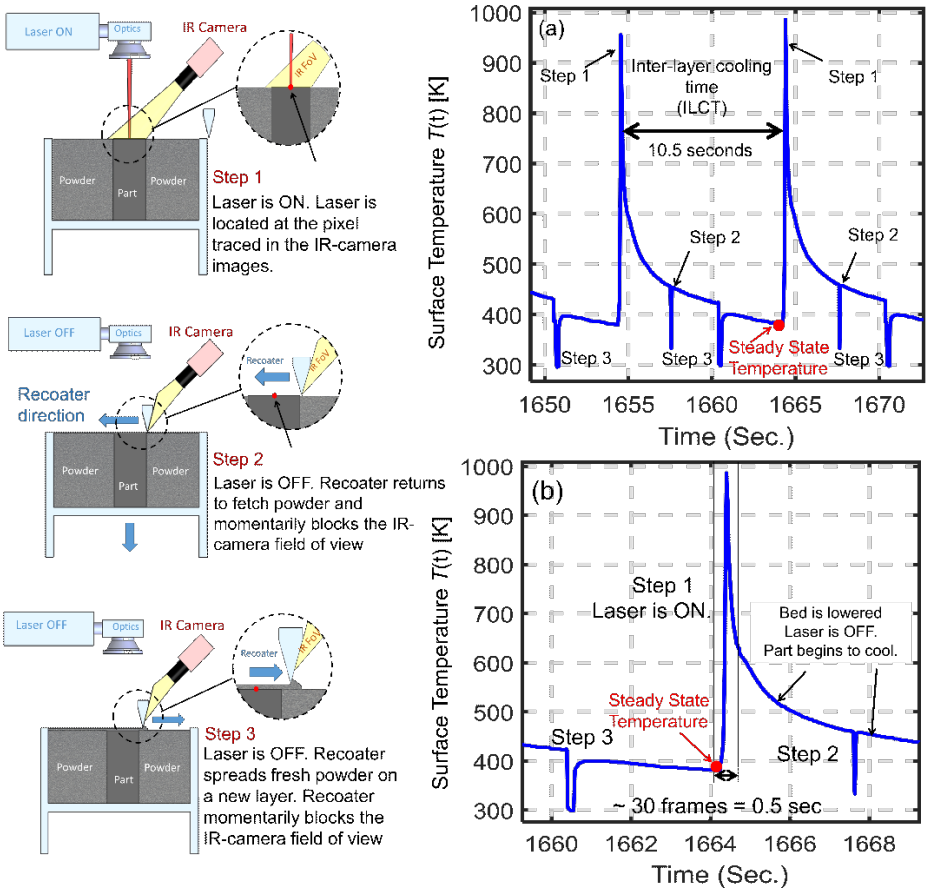

Figure 4. The physical process-related reasons for the spikes observed in the thermal camera images. (a) The three large periodic spikes in the temperature and the schematic representation of why these spikes occur. (b) zoomed in portion of the thermal camera signature.

2.4 Procedure for Application of the Graph Theory Approach

The graph theory approach is illustrated schematically in Figure 5 in the context of Build 1. These steps are discussed in detail in our previous works [9, 18]. The graph theory approach, as explained in our previous work, converts the part geometry into a set number of discrete nodes [9]. A network graph is constructed over these nodes, and heat diffusion over the graph is studied layer-by-layer.

If the temperature at each node is arranged in matrix form, the instantaneous temperature $\mathbf{T}$ after time t is obtained as a function of the Laplacian eigenvectors ($\boldsymbol{\phi}$) and eigenvalues ($\boldsymbol{\Lambda}$), with T_0 as the melting point of the material,

$$\mathbf{T} = \boldsymbol{\phi} e^{-\alpha g \boldsymbol{\Lambda} t} \boldsymbol{\phi}' \; T_0 \qquad (1)$$

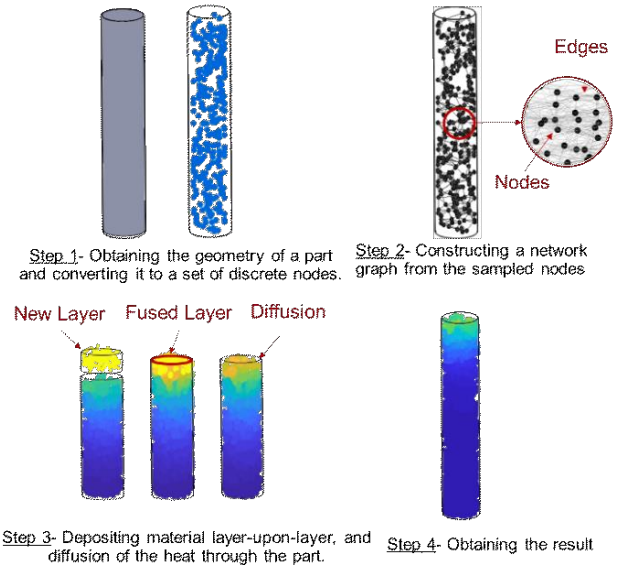

Figure 5. The four steps in the graph theory approach as applied to the cylindrical part described in Build 1. The mathematical details are described in [9].

a. Reducing computation time by simulating deposition of multiple layers at once (super layer)

To mitigate the computation time, instead of simulating the deposition one individual layer (layer height 50 μm) at a time, we simulate the deposition of several layers at a time. Such a layer consolidated from two or more individual layers is called a *super layer*. This super layer approach was described in our previous work, which showed that the thermal-induced distortion predicted using finite element models with the simulated layer thickness corresponding to 8 actual layers is within 5% of experimentally measured distortion measurements [19]. Using the super layer approach is particularly well suited to the graph theory method as the precision is independent of the simulated time step. This is because the time t for which the heat is diffused in the part in Eqn. (1) can be set to any continuous value in graph theory, without the need for discrete steps as in finite element analysis. The thickness of the super layer in this work in varied from 3 mm (consisting of 60 individual layers of 50 μm each) to 0.3 mm (6 individual layers).

b. Tuning the graph theory model parameters

The graph theory simulation studies require tuning of two types of factors.

(1) *Number of Nodes (N)*: The total number of nodes into which the part is discretized. In our previous work, we reported that selecting the number of nodes involves a tradeoff in computation time and accuracy [9]. For a complex geometry part, selecting a higher number of nodes was found to result in a smaller error in comparison to benchmark finite element studies, while degrading the computational efficiency. In this work, we evaluated the effect of varying the number of nodes from 1000 to 5000 in steps of 1000.

(2) *Model Parameters related to heat diffusion.* In the graph theory approach two model parameters must be determined, namely, the gain factor (g) Eqn. (1), and the neighborhood distance (ε) which governs the connectivity of the nodes [9]. There is an interaction between these two parameters. To mitigate this complexity, and need for extensive tuning, in this work we have made one change to the graph theory model, instead of setting ε to an absolute distance in mm, we now connect the nearest 50 neighbors of a node with edges. The number 50 is selected from extensive offline studies.

We report the mean absolute percentage error (MAPE) and root mean square error (RMSE, Kelvin) for each tested combination of super layer thickness and number of nodes. To obtain the gain factor (g), we fixed the total number of nodes at 1000, and conduct a grid search with respect to the infrared thermal measurements obtained for Phase 1 of Build 1. To make the calibration more rigorous, the layer height set in the simulation for the calibration of g studies is 50 μm, which is the same as the layer height of the build – the super layer is equal to actual layer height.

The value of g is changed with the number of nodes (N) fixed at 1000, and layer thickness 50 μm and the graph theory approach is applied for the first 20 mm of the build height the cylinder, i.e., the graph theoretic model is calibrated for the temperature readings from Phase 1 of Build 1.

The results from the model calibration procedure are shown in Figure 6(a). The value of g that minimizes the MAPE and RMSE is selected. The results from the grid search are shown in Figure 6(b). The value of g that minimizes MAPE and RMSE after the grid search was found to be 1.5×10^4; this value of g is set constant for all subsequent simulation studies, including Phase 2 and Phase 3 of Build 1, as well as the entirety of Build 2. The rest of the material-related constants and simulation parameters are described in Table 2. The simulations were conducted in the MATLAB environment on a desktop personal computer with an Intel Core i7-6700 CPU, clocked at 3.40 GHz with 32 gigabytes of onboard memory.

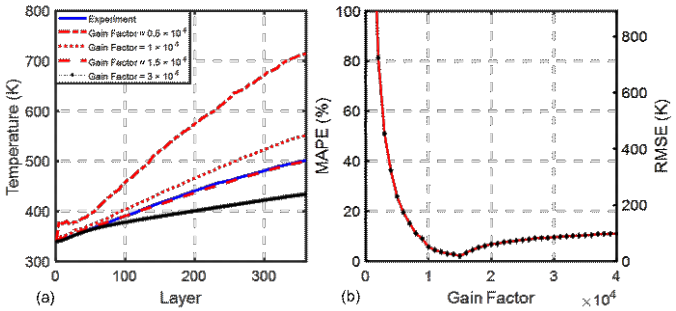

Figure 6. (a) Representative surface temperature trends obtained for Phase 1 of Build 1 by varying the gain factor (g). (b) The mean absolute percentage error and root mean squared error (RMSE, in Kelvin).

3 Results

3.1 Results for Build 1

The raw thermal signatures recorded for Build 1 are shown in *Figure 7*(a). These changes in the temperature trend are more clearly evident in *Figure 7*(b) on pre-processing of the raw temperature signatures as described in Sec. 2.3. A steady increase in temperature is observed during Phase 1, succeeded by a sharp increase observed at the start of Phase 2, and finally followed by a drop at the start of Phase 3. The frequency changes in the temperature correspond to the change ILCT; the reason for the sharp increase in temperature in Phase 2 is the decreased ILCT of roughly 6.6 seconds (*Figure 7*(d)), compared to 10.5 seconds in Phase 1 and Phase 3 (*Figure 7*(c)).

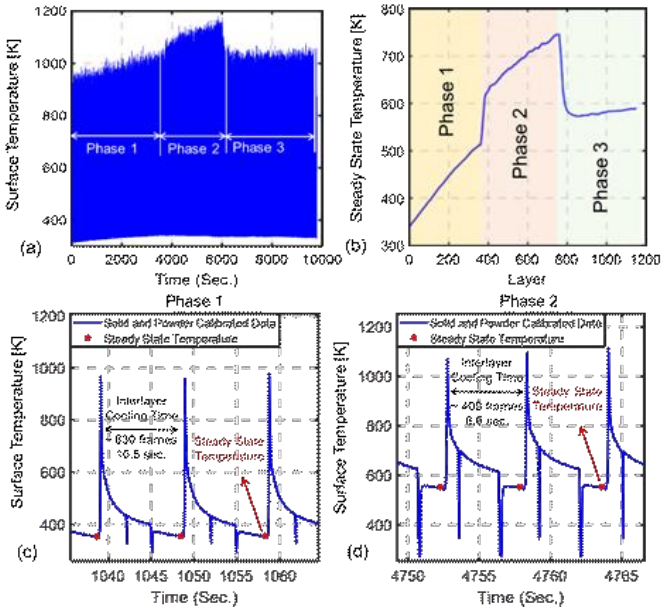

Figure 7. Data obtained from Build 1. (a) the raw temperature readings scaled by the LWIR camera, (b) smoothened trends obtained after removing the peaks and averaging the temperature in the time between sintering of two consecutive layers. (c) and (d) the interlayer cooling time decreases between Phase 1 and Phase 2 of the build leading to a large increase in steady state temperature

a. Comparison of graph theory predictions with experimental observations

In Figure 9(a), the effect of changing the super layer thickness (SLT) for a set number of graph nodes (N) of 3000 is mapped, and in Figure 9(b), the converse case, i.e., the SLT is maintained constant (0.3 mm, 6 individual layers of 50 µm each) and the surface temperature distribution with varying node density is observed. In general, as depicted in Figure 8 the accuracy improves (MAPE and RMSE reduce) as the SLT is decreased, and N is increased. However, the relationship is not linear, especially, given that the shape of the test geometry is a simple cylinder; the number of nodes does not tend to have a large effect. In the best-case scenario, a balance in both accuracy and computation time is obtained by setting the SLT at a level of 0.3 mm (6 individual layers) and maintaining the total number of nodes N = 3000. The error under these conditions (MAPE) is close to 6%, and the results are obtained in approximately 26 minutes (≈ 1/6th of the actual build time of 171 minutes).

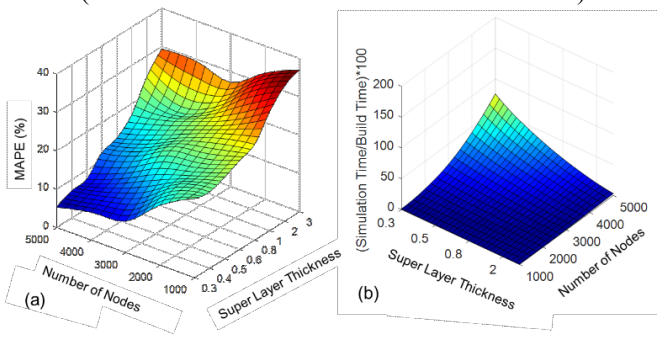

Figure 8: Sensitivity analysis for Build 1. (a)The effect of the super layer thickness (SLT) in mm and number of nodes (N) used in the graph theory approach on the error vis-à-vis experimental data. (b) The ratio of the simulation time to build time as a percentage, versus N and SLT. The decrease in SLT and increase in number of nodes (N) improves the prediction accuracy, at the cost of computation time.

Table 2. Summary of the simulation parameters used in this work

Simulation Parameters	**Values**
Super layer thickness [mm]	Varies from 3 to 0.3 mm for Build 1 (Cylinder) and from 1 to 0.2 mm for Build 2 (Inverted Cone)
Total number of nodes in the part (N)	Varies from 1000 to 5000 in steps of 1000
Node Density (N per mm^3)	Varies from 0.3 to 1.6 for Build 1 (Cylinder) and from 0.8 to 4.3 for Build 2 (Inverted Cone)
Number of neighbors which is connected to each node.	50
Gain factor (g)	1.3×10^4
Convection coefficient wall to powder, h_w [W·m^{-2}· K]	1×10^{-5}
Convection coefficient substrate (sink), h_s [W·m^{-2}· K]	1×10^{-2}
Thermal diffusivity (α), [m^2/s]	3×10^{-6}
Density, ρ [kg/m^3]	8,440
Melting Point (T_0) (K)	1,600
Ambient temperature, T_∞ (K)	300
Processing hardware	Intel Core i7-6700 CPU, @3.40 GHz with 32 GB RAM.

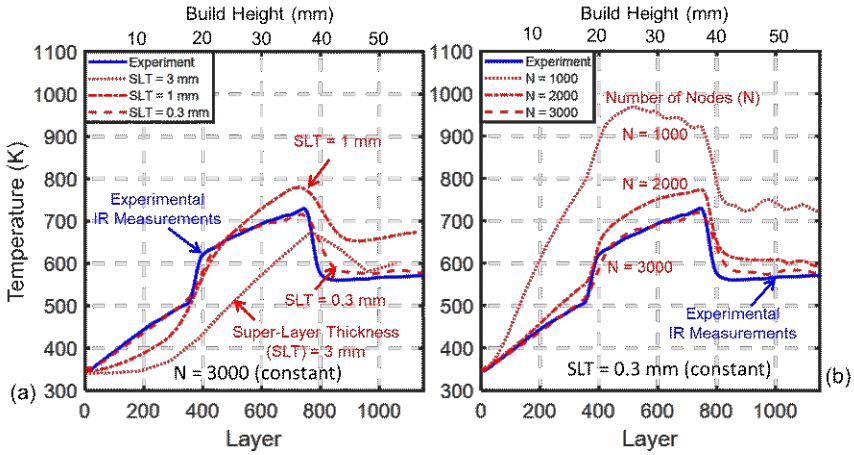

Figure 9. (a) Representative temperature trend predictions for Build 1 (cylinder). The effect of the super layer thickness on the temperature trends predicted using graph theory with number of nodes fixed at N = 3000. (b) The effect of varying the number of nodes N at a fixed super layer thickness of 0.3 mm (6 actual layers of 50 μm each). The best results are obtained with N = 3000 and super layer thickness set at 0.3 mm. The computation time is ~ 27 minutes with the resulting mean absolute percentage error close to 6%

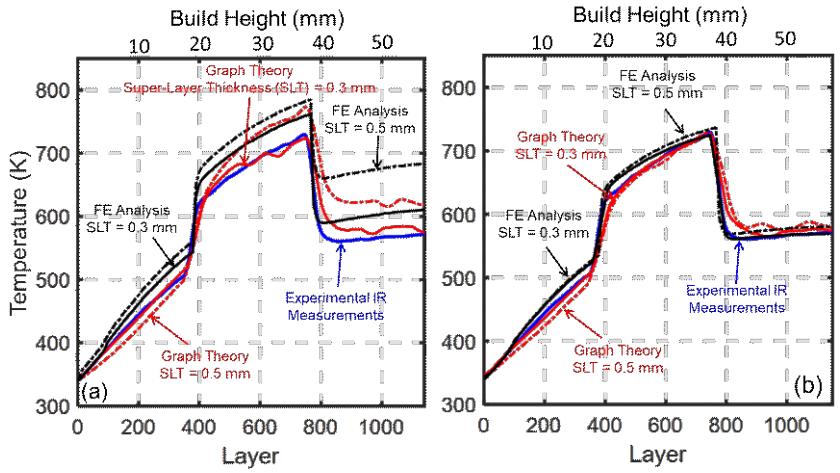

Figure 10. The finite element and graph theory results compared for different super layer thicknesses (SLT) for Build 1. The number of nodes for the graph theoretic approach are fixed at (a) N=3000 and (b) = 5000. Abaqus is used for simulating the deposition of super layers in the FE approach.

Table 3. Comparison of finite element and graph theoretic approaches for Build 1 (cylinder). The actual build time is 171 minutes (10,260 seconds)

	Finite Element		Graph Theory		Graph Theory		Finite Element		Graph Theory	
Nodes (N)	3000		3000		4000		5000			
Super Layer Thickness (SLT) [mm]	0.3	0.5	0.3	0.5	0.3	0.5	0.3	0.5	0.3	0.5
Computation Time [s]	2,048	1,347	1,655	949	3,912	2,209	10,446	6,053	7,270	4,176
MAPE (%)	16.7	29.4	13.8	18.2	8.7	11.5	9.1	9.4	8.6	10.4
RMSE (Kelvin, [K])	36.8	90.1	16.2	54.1	15.7	16.8	17.2	18.4	15.2	25.1

b. Comparison of graph theory predictions with finite elements analysis

The predictions from the graph theory approach are compared with finite element (FE) analysis in Figure 10 and Table 3. To ensure equitable comparison, we implemented the coarse super layer approach in a finite element framework in the commercially available Abaqus software, the detailed implementation of the FE analysis is described in Ref. [19].

In Figure 10(a), representative thermal trends for two super layer settings 0.3 mm (6 individual layers) and 0.5 mm (8 individual layers), with N = 3000 for the graph theoretic approach are compared with FE analysis (approximately 3000 nodes) and experimental temperature measurements. The results for N = 5000 are shown in Figure 10(b).

With N =3000, and super layer thickness (SLT) 0.3 mm, the MAPE for the FE analysis is approximately 16%, and the results are obtained within 2,048 seconds (34 minutes). Using the graph theory approach, the MAPE is 14%, and the trends are obtained in 1,655 seconds (27 minutes) of computation.

Next, we fix the MAPE of ~ 9% , and RMSE 16.5 ± 1 K and compare the computational time for graph theory and FE approach for an identical resolution (SLT = 0.3). For the graph

theory approach the MAPE and RMSE reduced to less than 9% and 16 K on increasing N = 4000 with corresponding computation time of 65 minutes.

To achieve the same level of prediction error it requires the FE approach 5000 nodes, and nearly 175 minutes. Effectively, the graph theory approach requires 40% of the computation time of FE to reach approximately similar level of MAPE and RMSE with an identical level of resolution (super layer thickness). The computational advantage of the graph theory approach is retained when the number of nodes N = 5000 for both FE and graph theory; the graph theory approach converges ~30% faster than FE.

3.2 Results for Build 2

a. Thermal signatures acquired from the thermal camera

The procedure described earlier in Sec. 2.3 is used to pre-process the thermal signatures obtained for Build 2. As shown in *Figure 11*(a), in Build 2, a gradual increase in temperature is observed at the top surface after removing the peaks in the thermal signature. This geometry also has the effect of increasing the ILCT with the build height (*Figure 11*(b)), because, as the top surface area increases, the time required to scan successive layers also increases.

The increasing trend in surface temperature is gradual, almost linear, as the accumulation of heat near the top surface is concurrently accompanied by an increase in ILCT. In other words, while the temperature increases for layers near the top, there is also more time for the layer to cool because it takes longer time for the laser to scan a larger surface area.

b. Comparison of graph theory predictions with experimental observations

The inverted cone shape is more complex than the cylinder, in that the cross-section area changes with the build height, and hence more number of nodes are required to capture the heat flux. As before, a smaller super layer thickness (SLT) and larger number of nodes both improve the accuracy of the solution. A representative best case scenario is shown in Figure 12, which shows the effect of the super layer thickness and number of nodes (N) on the surface temperature trends predictions from graph theory.

For instance, in Figure 12 when the number of nodes (N) is set at 4000, and the SLT is 0.3 mm the MAPE ~ 9%, and computation time is close to 34 minutes. Another situation with similar results is to set the super layer thickness at 0.2 mm with N = 4000, which results in MAPE ~ 8%, and computation time 41 minutes. The actual build time for Build 2 is close to 51 minutes.

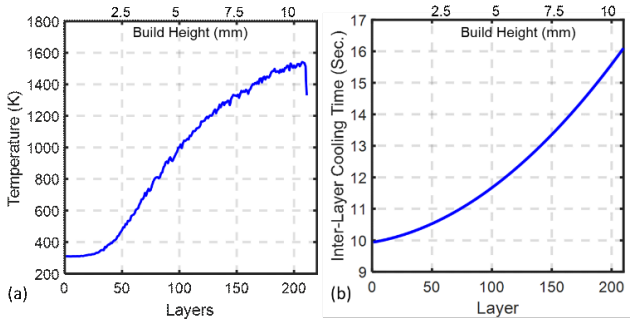

Figure 11. (a) The gradual increase in the surface temperature, as well as (b) the interlayer cooling time with the build height. We note in (a) that the IR camera is calibrated in the range of room temperature (300 K) to 800 K.

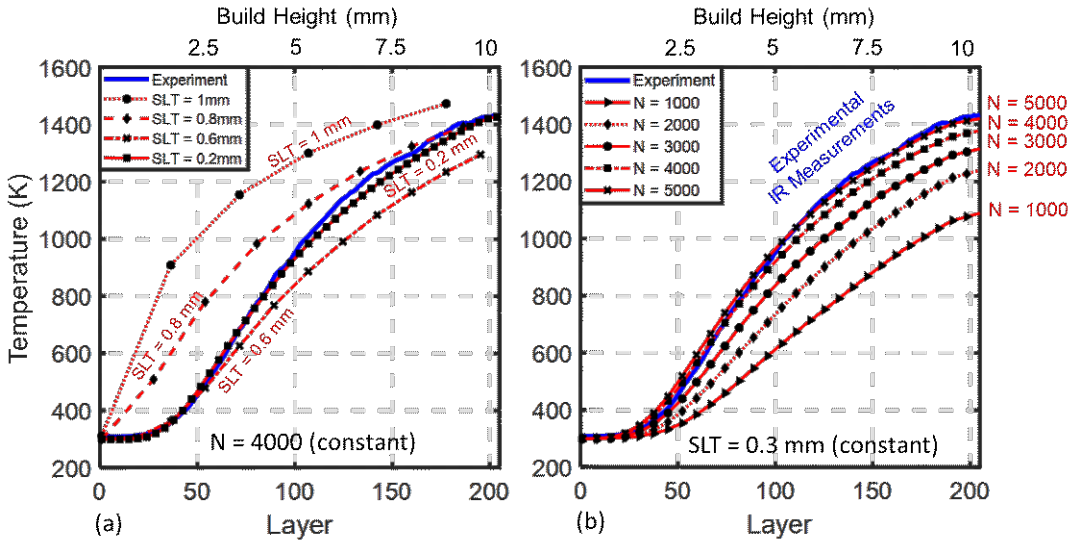

Figure 12. (a) Representative temperature trend predictions for Build 2 (inverted cone). The effect of the super layer thickness on the temperature trends predicted using graph theory with number of nodes fixed at N = 4000. (b) The effect of varying the number of nodes N at a fixed super layer thickness of 0.3 mm (6 actual layers of 50 μm each). The best results are obtained with N = 4000 and super layer thickness (SLT) set at either 0.3 mm or 0.2 mm. The computation time for N=4000 and SLT = 0.3 mm is ~ 34 minutes with the resulting mean absolute percentage error (MAPE) close to 9%; for SLT = 0.2 mm the computation time is 41 minutes and MAPE ~ 8%.

c. Comparison of graph theory predictions with finite element analysis

The graph theory-derived predictions for Build 2 are compared with the FE analysis in Figure 13 and Table 4. For equitable comparison, the FE analysis is set to a super layer thickness of 0.2 mm and 0.3 mm, and the number of nodes (N) is set at 4000. As apparent from Figure 13(a), both the FE and graph theory approaches track the increasing surface temperature trends evident in the experimental data. Furthermore, for the results shown in Figure 13 (b) we increased number of nodes (N) for the FE analysis until it converged to a nearly identical accuracy level of accuracy in terms of MAPE and RMSE observed for graph theory.

As exemplified in Figure 13, and quantitatively in Table 4, for a fixed resolution (SLT), and for an RMSE of 28.5 ± 1 K, and MAPE ~ 6%, the FE analysis required N = 6800 and 96 minutes of computation time. By contrast, for the foregoing degree of prediction error, the graph theory approach required N = 4000, and converged in 41 minutes. In other words, the graph theory required 40% fewer nodes and converged within 40% of the time required by FE. These results affirm the computational advantages of the graph theory approach over FE.

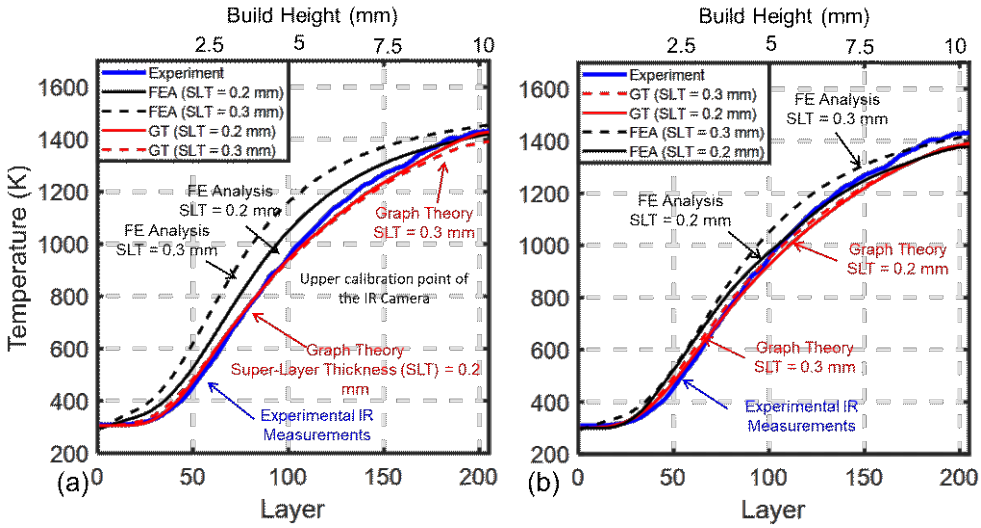

Figure 13. The finite element and graph theory results compared for different super layer thicknesses for Build 2. The number of nodes for the graph theoretic approach are fixed at N=4000. Abaqus is used for simulating the deposition of super layers in the FE analysis.

Table 4. Comparison of finite element and graph theoretic approaches for Build 2 (inverted cone).

	Finite Element		Graph Theory		Graph Theory		Finite Element	
Number of nodes (N)	4000		4000		5000		6800	
Super Layer Thickness (mm)	0.2	0.3	0.2	0.3	0.2	0.3	0.2	0.3
Computation Time [s]	3,274	2,948	2,471	2,081	4,784	4,045	5,982	5,034
MAPE (%)	9.6	15.9	5.73	6.8	3.72	4.54	6.2	10.9
RMSE [K]	42.1	76.4	26	32.8	12.15	20.7	27.6	43.8

4 Conclusions

This work provided the experimental evidence to substantiate the computational efficiency and accuracy of the graph theoretic approach proposed in our previous work [9]. We arrive at the following conclusions through two experimental builds conducted in the specific context of the laser powder bed fusion (LPBF) AM process.

(1) In Build 1, a cylindrical part was built in a phased manner, such that the interlayer cooling time changed on account of other parts being present during the build. In the best case scenario, the graph theoretic approach predicted the temperature history within 25 minutes with a mean absolute percentage error (MAPE) less than 7% and root mean squared error the actual build time was close to 171 minutes. For a comparable level of accuracy, a coarse finite element approximation requires 34 minutes and MAPE exceeding 10%.

From a practical perspective, Build 1 shows that the graph theoretic approach is capable of emulating a complex multi-part build plan with test parts being removed and added during the process. Furthermore, the graph theoretic approach has a large degree of flexibility, as the approach can be scaled to provide finer hatch-level information as shown in our previous work, or made coarser by simulating deposition of several individual layers consolidated together (called a super layer) [9].

(2) In Build 2, a conical part was built such that the diameter of its circular end progressively increases with the build height (an inverted cone). The test geometry depicts an increase in the surface temperature despite processing under constant

LPBF parameters. The graph theoretic approach predicted the surface temperature distribution with an error less than 8% of the experimental observations within 35 minutes (actual build time 51 minutes). In contrast, for a comparable level of accuracy (9%), the finite element approach requires 55 minutes.

In our forthcoming works we will endeavor to validate the graph theory approach for large, complex geometry parts, and further, characterize the effect of the temperature distribution on microstructure and distortion.

Acknowledgments

One of the authors (PKR) thanks the NSF for funding his research through the following grants CMMI-1719388, CMMI-1739696, MRI 1920245, CMMI-1752069, and OIA 929172 at University of Nebraska-Lincoln. Specifically, the concept of using spectral graph theory for modeling in metal additive manufacturing applications was funded through CMMI-1752069. We also thank the NSF INTERN program (Dr. P. Balan) for providing supplemental funding for Reza Yavari to spend six months at Edison Welding Institute.

References Cited

[1] Francois, M. M., Sun, A., King, W. E., Henson, N. J., Tourret, D., Bronkhorst, C. A., Carlson, N. N., Newman, C. K., Haut, T., Bakosi, J., Gibbs, J. W., Livescu, V., Vander Wiel, S. A., Clarke, A. J., Schraad, M. W., Blacker, T., Lim, H., Rodgers, T., Owen, S., Abdeljawad, F., Madison, J., Anderson, A. T., Fattebert, J. L., Ferencz, R. M., Hodge, N. E., Khairallah, S. A., and Walton, O., 2017, "Modeling of additive manufacturing processes for metals: Challenges and opportunities," Current Opinion in Solid State and Materials Science, 21(4), pp. 198-206.doi:https://doi.org/10.1016/j.cossms.2016.12.001

[2] DebRoy, T., Wei, H. L., Zuback, J. S., Mukherjee, T., Elmer, J. W., Milewski, J. O., Beese, A. M., Wilson-Heid, A., De, A., and Zhang, W., 2018, "Additive manufacturing of metallic components – Process, structure and properties," Progress in Materials Science, 92, pp. 112-224.doi:https://doi.org/10.1016/j.pmatsci.2017.10.001

[3] Denlinger, E. R., Gouge, M., and Michaleris, P., 2018, Thermo-Mechanical Modeling of Additive Manufacturing, Butterworth-Heinemann.

[4] Bandyopadhyay, A., and Traxel, K. D., 2018, "Invited Review Article: Metal-additive manufacturing—Modeling strategies for application-optimized designs," Additive Manufacturing

[5] Foteinopoulos, P., Papacharalampopoulos, A., and Stavropoulos, P., 2018, "On thermal modeling of Additive Manufacturing processes," CIRP Journal of Manufacturing Science and Technology, 20, pp. 66-83.doi:https://doi.org/10.1016/j.cirpj.2017.09.007

[6] Schoinochoritis, B., Chantzis, D., and Salonitis, K., 2015, "Simulation of metallic powder bed additive manufacturing processes with the finite element method: A critical review," Proceedings of the Institution of Mechanical Engineers, Part B: Journal of Engineering Manufacture, 231(1), pp. 96-117.doi:10.1177/0954405414567522

[7] Sames, W. J., List, F., Pannala, S., Dehoff, R. R., and Babu, S. S., 2016, "The metallurgy and processing science of metal additive manufacturing," International Materials Reviews, 61(5), pp. 315-360.doi:10.1080/09506608.2015.1116649

[8] Knapp, G. L., Mukherjee, T., Zuback, J. S., Wei, H. L., Palmer, T. A., De, A., and DebRoy, T., 2017, "Building blocks for a digital twin of additive manufacturing," Acta Materialia, 135, pp. 390-399.doi:https://doi.org/10.1016/j.actamat.2017.06.039

[9] Yavari, M. R., Cole, K., and Rao, P., 2019, "Thermal Modeling in Metal Additive Manufacturing using Graph Theory," ASME Transactions, Journal of Manufacturing Science and Engineering, 141(7), pp. 071007-071027.doi:10.1115/1.4043648

[10] Goldak, J., Chakravarti, A., and Bibby, M., 1984, "A new finite element model for welding heat sources," Metallurgical Transactions B, 15(2), pp. 299-305.doi:10.1007/bf02667333

[11] Goldak, J. A., and Akhlaghi, M., 2005, "Computer simulation of welding processes," Computational Welding Mechanics, pp. 16-69

[12] Williams, R. J., Piglione, A., Rønneberg, T., Jones, C., Pham, M.-S., Davies, C. M., and Hooper, P. A., 2019, "In-situ thermography for laser powder bed fusion: effects of layer temperature on porosity, microstructure and mechanical properties.," Additive Manufacturing, 30(22), pp. 416-425.doi:https://doi.org/10.1016/j.addma.2019.100880

[13] King, W., Anderson, A., Ferencz, R., Hodge, N., Kamath, C., Khairallah, S., and Rubenchik, A., 2015, "Laser powder bed fusion additive manufacturing of metals; physics, computational, and materials challenges," Applied Physics Reviews, 2(4), p. 041304

[14] Wang, X., and Chou, K., 2018, "Effect of support structures on Ti-6Al-4V overhang parts fabricated by powder bed fusion electron beam additive manufacturing," Journal of Materials Processing Technology, 257, pp. 65-78.doi:https://doi.org/10.1016/j.jmatprotec.2018.02.038

[15] Cooper, K., Steele, P., Cheng, B., and Chou, K., 2018, "Contact-Free Support Structures for Part Overhangs in Powder-Bed Metal Additive Manufacturing," Inventions, 3(1).doi:10.3390/inventions3010002

[16] Bikas, H., Lianos, A. K., and Stavropoulos, P., 2019, "A design framework for additive manufacturing," The International Journal of Advanced Manufacturing Technology.doi:10.1007/s00170-019-03627-z

[17] Boone, N., Zhu, C., Smith, C., Todd, I., and Willmott, J. R., 2018, "Thermal near infrared monitoring system for electron beam melting with emissivity tracking," Additive Manufacturing, 22, pp. 601-605.doi:https://doi.org/10.1016/j.addma.2018.06.004

[18] Yavari, M. R., Cole, K. D., and Rao, P. K., 2019, "Design Rules for Additive Manufacturing – Understanding the Fundamental Thermal Phenomena to Reduce Scrap," Procedia Manufacturing, 33, pp. 375-382.doi:https://doi.org/10.1016/j.promfg.2019.04.046

[19] Williams, R. J., Davies, C. M., and Hooper, P. A., 2018, "A pragmatic part scale model for residual stress and distortion prediction in powder bed fusion," Additive Manufacturing, 22, pp. 416-425.doi:https://doi.org/10.1016/j.addma.2018.05.038

